

---

# p<sup>3</sup>VAE: A PHYSICS-INTEGRATED GENERATIVE MODEL

## APPLICATION TO THE SEMANTIC SEGMENTATION OF OPTICAL REMOTE SENSING IMAGES

---

|  |   |  |
|--|---|--|
| <b>Romain Thoreau</b><br>romain.thoreau@onera.fr             | <b>Laurent Risser</b><br>lrissier@math.univ-toulouse.fr | <b>Véronique Achard</b><br>veronique.achard@onera.fr |
| <b>Béatrice Berthelot</b><br>beatrice.berthelot@magellium.fr | <b>Xavier Briottet</b><br>xavier.briottet@onera.fr      |  |

### ABSTRACT

The combination of machine learning models with physical models is a recent research path to learn robust data representations. In this paper, we introduce p<sup>3</sup>VAE, a generative model that integrates a perfect physical model which partially explains the true underlying factors of variation in the data. To fully leverage our hybrid design, we propose a semi-supervised optimization procedure and an inference scheme that comes along meaningful uncertainty estimates. We apply p<sup>3</sup>VAE to the semantic segmentation of high-resolution hyperspectral remote sensing images. Our experiments on a simulated data set demonstrated the benefits of our hybrid model against conventional machine learning models in terms of extrapolation capabilities and interpretability. In particular, we show that p<sup>3</sup>VAE naturally has high disentanglement capabilities. Our code and data have been made publicly available at <https://github.com/Romain3Ch216/p3VAE>.

## 1 Introduction

Hybrid modeling, that is the combination of data-driven and theory-driven modeling, has recently raised a lot of attention. The integration of physical models in machine learning has indeed demonstrated promising properties such as improved interpolation and extrapolation capabilities and increased interpretability [1, 2]. Conventional machine learning models learn correlations, from a training data set, in order to map observations to targets or latent representations, with the hope to generalize to new data. In other words, machine learning models implicitly make assumptions on the training data distribution that shall hold true on the real data distribution. We will refer to those assumptions as inductive biases [3, 4], that usually do not generalize in small data regime [5]. In contrast, hybrid models are partially grounded on deductive biases, *i.e.* assumptions derived, in our context, from physics models that generalize, by nature, to out-of-distribution data. Therefore, in various fields for which the data distribution is governed by physical laws, such as fluid dynamics, thermodynamics or solid mechanics, hybrid modeling has recently become a hot topic [6, 7, 8].

In the present paper, we introduce p<sup>3</sup>VAE, a physics-integrated generative model that combines a perfect physical model with a machine learning model. p<sup>3</sup>VAE aims to decouple the variation factors that are intrinsic to the data from physical factors related to acquisition conditions. On the hypothesis that acquisition conditions induce complex and non-linear data variations, we argue that a conventional generative model would hardly decorrelate intrinsic factors from physical factors. Therefore, we introduce deductive physics-based biases in the decoding part of a semi-supervised variational autoencoder. Variational AutoEncoders (VAEs) [9] are powerful latent variable probabilistic models that have an autoencoder framework. The key to their success lies in their stochastic variational inference and learning algorithm that allows to leverage very large unlabeled data sets and to model complex posterior data distributions given latent variables [9]. Besides, recent advances offer more and more control on the latent space distributions [10, 11, 12, 13]. VAEs were used, for instance, in text modeling to capture topic information as a Dirichlet latent variable [14] or in image modeling where latent variables were both discrete and continuous [15].

---

This paper is submitted to the International Journal of Computer Vision.

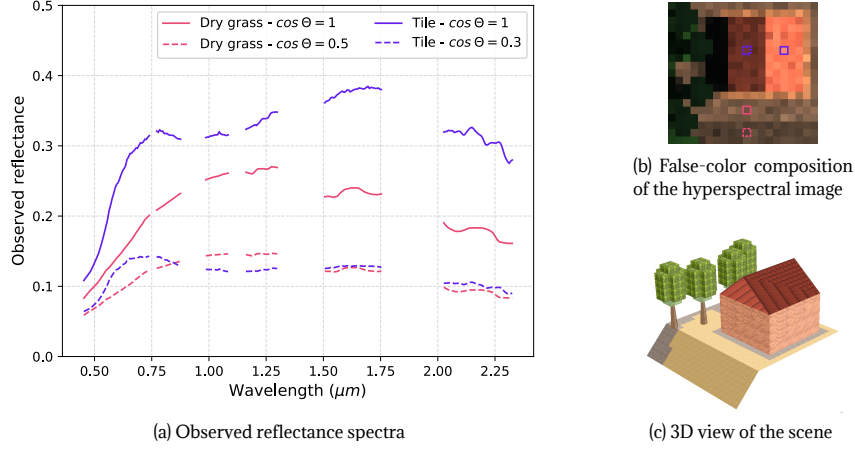


Figure 1: Illustration of intra-class variabilities and inter-class similarities due to different pixel-wise irradiance conditions.  $\Theta$  is the solar incidence angle. The lower is  $\Theta$ , the higher is the direct irradiance.

Integrating physics in an autoencoder was first proposed by [16]. They used a fully physical model in place the decoder to inverse a 2D exponential light galaxy profile model. [2] generalized the work of [16] by developing a mathematical formalism introduced as physics-integrated VAEs. Physics-integrated VAEs ( $\phi$ -VAE) complement an imperfect physical model with a machine learning model in the decoder of a VAE. To have a consistent use of physics despite the high representation power of machine learning models, they employ a regularization strategy that is central to their contribution. In contrast, p<sup>3</sup>VAE integrates a **perfect** physics model that **partially** captures the factors of variations.

As an example of application, we apply p<sup>3</sup>VAE to the semantic segmentation of reflectance hyperspectral Earth observation images, which consists in labelling each pixel with a land cover class. Reflectance is a physical property of matter that can be estimated from remote sensing data. As an intrinsic property of the land cover, it is a relevant feature for semantic segmentation. However, without knowledge of the local (*i.e.* pixel-wise) irradiance conditions (that depend on topography), one material can have totally different reflectance estimates. Fig. 1 shows examples of reflectance spectra observations<sup>1</sup> for two materials with different local slopes (*i.e.* different irradiance). Those examples illustrate how wide and non-linear the spectral irradiance-based variability can be and how reflectance spectra from different classes can look alike in specific irradiance conditions. Additionally, the reflectance of one material can change based on various physical parameters such as its surface roughness, humidity or chemical composition (*e.g.* chlorophyll content of vegetation). We will refer to this kind of variability as intrinsic intra-class variability. Capturing the irradiance-based and the intrinsic intra-class variabilities in a supervised setting is very challenging because labeled remote sensing data is often scarce. Pixel annotations, especially for hyperspectral data, indeed require time-consuming photo-interpretation by experts and expensive field campaigns. Therefore, only few thousands pixels are usually labeled out of many millions, making supervised manifold learning often inefficient [17].

The main contributions of the paper are as follows:

- We introduce p<sup>3</sup>VAE, a hybrid model that combines conventional neural networks layers with physics-based layers for generative modeling,
- We define a semi-supervised training procedure to balance between physics and trainable parameters of p<sup>3</sup>VAE,
- We introduce an inference procedure to fully leverage the physics part of p<sup>3</sup>VAE,
- We apply our model to the semantic segmentation of hyperspectral remote sensing images and demonstrate the benefits of hybrid modeling in contrast with data-driven modeling in terms of classification accuracy, interpolation and extrapolation capabilities, disentanglement and latent variables interpretability.

Our paper is organized as follows. Section 2 discusses the related work. Section 3 presents our model in details. Section 4 describes the simulated data set. We present and discuss the experiments in section 5 and 6, respectively. Finally, we conclude in section 7.

<sup>1</sup>Here we use the term *observation* in its statistical sense.

## 2 Related work

Our method makes use, at the same time, of physical priors and of a semi-supervised learning technique, which is intrinsically linked to the architecture of p<sup>3</sup>VAE. Therefore, we review related work on hybrid modeling and semi-supervised learning.

### 2.1 Hybrid modeling

Hybrid modeling can be divided into physics-based losses [18, 19, 7, 1] and physics-based models, in which our method fits. Physics-based models, also named as physics-informed neural networks, embed physical layers in their design. [20] and [21] introduced VAEs which latent variables were grounded to physical quantities (such as position and velocity) and governed by Ordinary Differential Equations (ODEs). More related to our work, [16] solves an inverse problem by using a conventional autoencoder in which they substitute the decoder by a fully physical model. They demonstrated that the architecture of the decoder induces a natural disentanglement of the latent space. This model is a particular case of the formalism of physics-integrated VAEs introduced by [2], that is the most closely related work to our methodology. Physics-integrated VAEs ( $\phi$ -VAE) are variational autoencoders which decoders combine statistical and physical models. The key idea of [2] is that the combination of an imperfect physical model with a machine learning model gives more precise results than an imperfect physical model alone and better generalization performances than a machine learning model alone. More precisely, they showed that the deductive biases introduced by the physical model regularize the machine learning model, yielding more robust local optima. Because neural networks, with powerful representation power, could bypass the physical part to model the data, they introduced a specific training procedure. Their optimization scheme aims to balance the power of the neural network so that it models the residual error of the physics model.  $\phi$ -VAEs will be described and discussed in details in section 6.4. While some semi-supervised techniques use unlabeled data to regularize a machine learning model, hybrid modeling can be seen as a form of regularization that discard machine learning models that contradict the physics model.

Close but outside the scope of hybrid modeling are methods that disentangle the latent space to have semantically meaningful latent variables. For instance, [22] introduced a stochastic gradient variational Bayes training procedure to encourage latent variables of a VAE to fit physical properties (rotations and lighting conditions of 3D rendering of objects). Other state-of-the-art disentanglement techniques such as [23, 24, 25] can yield interpretable latent spaces, for instance on the MNIST data set [26], where latent variables represent the rotations or the thickness of handwritten digits.

### 2.2 Semi-supervised learning

Semi-supervised techniques exploit the structure of unlabeled data, in addition to scarce labeled data, to learn data manifolds. Van Engelen and Hoos provide an exhaustive survey on transductive and inductive semi-supervised methods in [27]. As far as transductive methods optimize over the predictions themselves, we only focus on inductive methods that optimize over predictive models, to which we can integrate some prior knowledge. Common inductive techniques include pseudo-labeling, or self-labeled, approaches [28] (where the labeled data set is iteratively enlarged by the predictions of the model), unsupervised preprocessing (such as feature extraction with contractive autoencoders [29] or pretraining [30]) and regularization techniques on the unlabeled data. Regularization includes (along side a classification loss) additional reconstruction losses on embedding spaces [31, 32], manifold regularization [33], perturbation-based approaches such as virtual adversarial training [34] that decreases the predictions sensitivity to inputs noise or, in the context of semantic segmentation, relaxed k-means [35]. Finally, generative models are, by nature, relevant to handle unlabeled data. State-of-the-art generative models such as Generative Antagonist Nets (GANs) [36], VAEs [9] and normalizing flows [37] were enhanced to handle both labeled and unlabeled data. For instance, [38] introduced a semi-supervised version of InfoGAN [39]; [40] and [41] developed a methodology to train VAEs and normalizing flows in semi-supervised settings, respectively.

## 3 Method

### 3.1 General framework

Our model builds on the concept of physics-integrated VAEs [2]. In this section, we describe the architecture of our model, its optimization scheme and inference procedure.

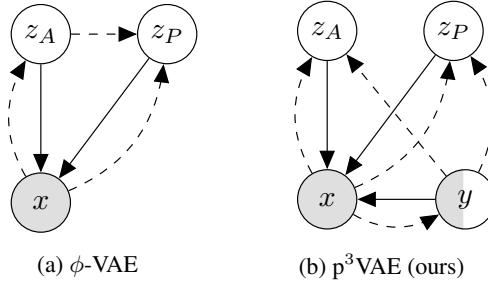


Figure 2: Graphical model representations of (a)  $\phi$ -VAE and (b)  $p^3$ VAE. Solid lines denote the generative model (a)  $p_\theta(z_A, z_P)p_\theta(x|z_A, z_P)$  and (b)  $p_\theta(z_A, z_P, y)p_\theta(x|z_A, z_P, y)$ . Dashed lines denote the variational posterior approximation (a)  $q_\phi(z_A|x)q_\phi(z_P|x, z_A)$  and (b)  $q_\phi(y|x)q_\phi(z_A, z_P|x, y)$ . White nodes are latent variables while gray ones are observed variables.

### 3.1.1 p<sup>3</sup>VAE architecture

We assume that a data point  $x \in \mathcal{X}$  is generated by a random process that involves continuous latent variables  $z_A \in \mathcal{Z}_A$  and  $z_P \in \mathcal{Z}_P$  as well as discrete variables  $y \in \mathcal{Y}$  that are sometimes observed, and sometimes unobserved. We assume that the latent variable  $z_P$  is grounded to some physical properties while the latent variable  $z_A$  has no physical meaning.  $z_P$  could be, for instance, the pixel-wise irradiance mentioned in section 1.  $y$  is a categorical variable such as the class, for which we have annotations for a few data points.  $\mathcal{X}$ ,  $\mathcal{Y}$ ,  $\mathcal{Z}_A$  and  $\mathcal{Z}_P$  are subsets of the euclidean space.

The generative process consists of two steps: (1) values of  $z_A$ ,  $z_P$  and  $y$  are generated from a prior distribution  $p_\theta(z_A, z_P, y)$  parameterized by  $\theta$ ; (2) a value  $x$  is generated from the conditional distribution  $p_\theta(x|z_A, z_P, y)$ . We assume that latent variables  $z_A$ ,  $z_P$ ,  $y$  are independent factors of variations, *i.e.* that they are mutually independent:

$$p_\theta(z_A, z_P, y) := p_\theta(z_A)p_\theta(z_P)p_\theta(y) \quad (1)$$

Besides, we assume a Gaussian observation noise  $\Sigma$  and define the likelihood as follows:

$$p_\theta(x|z_A, z_P, y) := \mathcal{N}(x|f_P \circ f_A(z_A, z_P, y), \Sigma) \quad (2)$$

where  $f_A : \mathcal{Z}_A \times \mathcal{Y} \rightarrow \mathcal{X}$  is a neural network and  $f_P : \mathcal{Z}_P \times \mathcal{X} \rightarrow \mathcal{X}$  is a physics model differentiable with regard to its inputs.

$p^3$ VAE has similarities with the physics-integrated VAE ( $\phi$ -VAE) introduced by [2]. Both models are illustrated on Fig. 2. Their similarities and differences are further discussed in section 6.4.

We would like to maximize the marginal likelihood  $p_\theta(x, y)$  when  $y$  is observed and  $p_\theta(x)$  otherwise, which are unfortunately intractable. Therefore, we follow the state-of-the-art variational optimization technique introduced in [9] by approximating the true posterior  $p_\theta(z_A, z_P, y|x)$  by a recognition model  $q_\phi(z_A, z_P, y|x)$ . Furthermore, we assume that  $q_\phi(z_A, z_P|x, y)$  factorizes as follows:

$$q_\phi(z_A, z_P|x, y) := q_\phi(z_A|x, y)q_\phi(z_P|x, y) \quad (3)$$

The encoding part  $q_\phi(z_A, z_P, y|x)$  and the decoding part  $p_\theta(x|z_A, z_P, y)$  form a variational autoencoder (with parameters  $\theta$  and  $\phi$ ).

### 3.1.2 p<sup>3</sup>VAE semi-supervised training

We now explain how we adapted the semi-supervised optimization scheme introduced by [40] to the training of our model.

**Semi-supervised Model Objective.** The objective function derived by [40] for an observation  $x$  is twofold. First, when its label  $y$  is observed, the evidence lower bound of the marginal log-likelihood  $\log p_\theta(x, y)$  is:

$$\begin{aligned} -\mathcal{L}(x, y) &= \mathbb{E}_{q_\phi(z_A, z_P|x, y)} [\log p_\theta(x|z_A, z_P, y) + \log p_\theta(y) + \log p_\theta(z_P, z_A) - \log q_\phi(z_A, z_P|x, y)] \\ &\leq \log p_\theta(x, y) \end{aligned} \quad (4)$$

Second, when the label is not observed, the evidence lower bound of the marginal log-likelihood  $\log p_\theta(x)$  is:

$$\begin{aligned} -\mathcal{U}(x) &= \mathbb{E}_{q_\phi(z_A, z_P, y|x)} [\log p_\theta(x|z_A, z_P, y) + \log p_\theta(y) + \log p_\theta(z_P, z_A) - \log q_\phi(z_A, z_P, y|x)] \\ &= \sum_y q_\phi(y|x) (-\mathcal{L}(x, y)) + \mathcal{H}(q_\phi(y|x)) \leq \log p_\theta(x) \end{aligned} \quad (5)$$

where  $\mathcal{H}(q_\phi(y|x))$  denotes the entropy of  $y|x$ . Besides, we can note that the term  $\mathbb{E}_{q_\phi(z_A, z_P|x, y)}[\log p_\theta(z_A, z_P) - \log q_\phi(z_A, z_P|x, y)]$  in equation (4) is the Kullback-Leibler divergence between  $q_\phi(z_A, z_P|x, y)$  and  $p_\theta(z_A, z_P)$ .

The categorical predictive distribution  $q_\phi(y|x)$  only contributes in the second objective function (5). To remedy this, we use the trick of [40] which consists in adding a classification loss to the total objective function, so that  $q_\phi(y|x)$  also learns from labeled data. The final objective function is defined as follows:

$$\mathcal{J} := \sum_{x, y \sim \tilde{p}_l} [\mathcal{L}(x, y) - \alpha \log q_\phi(y|x)] + \sum_{x \sim \tilde{p}_u} \mathcal{U}(x) \quad (6)$$

where  $\tilde{p}_l$  and  $\tilde{p}_u$  are the empirical labeled and unlabeled data distribution, respectively, and  $\alpha$  is a hyper-parameter that controls the relative weight between generative and purely discriminative learning.

**Gradient stopping.** The machine learning model  $f_A$  generates data features from the categorical variable  $y$  and the continuous variable  $z_A$ . Because  $f_A$  has very poor extrapolation capabilities, some inconsistent values of  $(z_A, z_P, y)$  can lead to a good reconstruction of the training data. To mitigate this issue, we do not back-propagate the gradients with regard to  $f_A$  parameters when  $y$  is not observed.

### 3.1.3 Inference

At inference, [40] uses the approximate predictive distribution  $q_\phi(y|x)$  to make predictions. However, although the true predictive distribution  $p_\theta(y|x)$  is intractable, we can compute  $\arg \max_y p_\theta(y|x)$  if we are only interested in the class predictions. As a matter of fact, assuming that  $p_\theta(y)$  is uniform, we have from Bayes rule that:

$$p_\theta(y|x) = \frac{p_\theta(x|y)p_\theta(y)}{p_\theta(x)} \propto p_\theta(x|y) \quad (7)$$

Moreover, denoting  $[z_A, z_P]$  as  $z$ , which is independent from  $y$ , we can write that:

$$p_\theta(x|y) = \int p_\theta(x, z|y) dz = \int p_\theta(x|y, z)p_\theta(z) dz = \mathbb{E}_{z \sim p_\theta(z)} p_\theta(x|y, z) \quad (8)$$

Thus, we can perform Monte Carlo sampling to estimate  $p_\theta(x|y)$ . In order to decrease the variance of the estimation, we can sample  $z$  from  $q_\phi(z|x)$ , performing importance sampling as follows:

$$p_\theta(x|y) = \mathbb{E}_{z \sim q_\phi(z|x)} \frac{p_\theta(z)}{q_\phi(z|x)} p_\theta(x|y, z) = \mathbb{E}_{y^* \sim q_\phi(y|x)} \mathbb{E}_{z \sim q_\phi(z|x, y^*)} \frac{p_\theta(z)}{q_\phi(z|x)} p_\theta(x|y, z) \quad (9)$$

To our knowledge, this derivation of  $\arg \max_y p_\theta(y|x)$  has not yet been used in the context of semi-supervised VAEs. Besides, this derivation offers a convenient way to estimate the uncertainty over the inferred latent variables. We can easily compute the empirical standard deviation of the  $z^i$ 's where  $z^i \sim q_\phi(z|x, y^*)$  and  $y^* \sim q_\phi(y|x)$ .

## 3.2 Application of the model to optical remote sensing data

In this section, we apply our methodology to semantic segmentation of high resolution optical remote sensing data. We first describe the physical model and then introduce the design of the VAE.

### 3.2.1 The radiative transfer model

Remote sensing optical sensors measure spectral radiance, *i.e.* a radiant flux per unit solid angle, per unit projected area, per unit wavelength ( $\text{W} \cdot \text{sr}^{-1} \cdot \text{m}^{-2} \cdot \text{nm}^{-1}$ ). Spectral radiance, in the reflective domain, is dependant of sun irradiance, of the atmospheric composition as well as the land cover and comes from various sources (see the illustration of irradiance and radiance terms on fig. 3). In contrast, reflectance, that is the ratio of the reflected radiant flux on the incident radiant flux, only depends on matter chemical composition. Therefore, reflectance is a much more relevant feature for semantic segmentation. Atmospheric corrections code, such as COCHISE [42], aim to deduct the atmospheric contribution to the measured radiance and to estimate pixel-wise reflectance. In the following, we introduce the basics of radiative transfer on which atmospheric codes are based on. In particular, we will focus on hypothesis that yield poor reflectance estimates when they do not hold true.

As most atmospheric codes do, we assume that land surfaces are lambertian, *i.e.* that they reflect radiation isotropically. We express the reflectance, as it is commonly done in the literature, at wavelength  $\lambda$  of a pixel of coordinates  $(x, y)$  as  $\rho^{xy\lambda}$ :

$$\rho^{xy\lambda} = \frac{\pi R_{dir}^{xy\lambda}}{I_{tot}^{xy\lambda} \tau_{dir}^\lambda} \quad \text{with} \quad \begin{cases} R_{dir}^{xy\lambda} &= R_{tot}^{xy\lambda} - R_{env}^{xy\lambda} - R_{atm}^\lambda \\ I_{tot}^{xy\lambda} &= I_{dir}^{xy\lambda} + I_{dif}^{xy\lambda} + I_{coup}^{xy\lambda} + I_{refl}^{xy\lambda} \end{cases} \quad (10)$$

where (leaving the dependence to  $x, y$  and  $\lambda$  implicit):

- $R_{tot}$  is the radiance measured by the sensor,
- $R_{atm}$  is the portion of  $R_{tot}$  that is scattered by the atmosphere without any interactions with the ground,
- $R_{env}$  is the portion of  $R_{tot}$  that comes from the neighbourhood of the pixel,
- $R_{dir}$  is the portion of  $R_{tot}$  that comes from the pixel,
- $I_{dir}$  is the irradiance directly coming from the sun,
- $I_{dif}$  is the irradiance scattered by the atmosphere,
- $I_{coup}$  is the irradiance coming from the coupling between the ground and the atmosphere,
- $I_{refl}$  is the irradiance coming from neighbouring 3D structures.

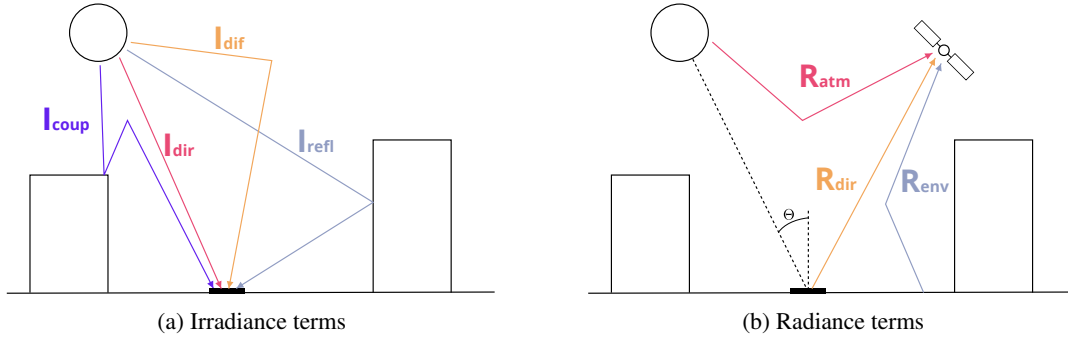


Figure 3: Illustration of the radiative components described in section 3.2.1. Figure reproduced from [43].

Those terms are illustrated on Fig. 3. More precisely,

$$I_{dir} = \delta_{dir} \cdot \cos \Theta \cdot I_{dir}^o \quad (11)$$

where  $\delta_{dir}$  is the portion of pixel directly lit by sun,  $\Theta$  is the solar incidence angle (*i.e.* the angle between the sun direction and the local normal) and  $I_{dir}^o$  is the direct irradiance for  $\delta_{dir} = 1$  and  $\Theta = 0$ .  $I_{dif}$  can be approximated by:

$$I_{dif} = \Omega \cdot p_\Theta \cdot I_{dif}^o \quad (12)$$

where  $\Omega$  is the sky viewing angle factor,  $p_\Theta$  is a correction coefficient that accounts for the anisotropy of the diffuse irradiance and  $I_{dif}^o$  is the diffuse irradiance for a pixel on a horizontal ground with  $\Omega = 1$  (*i.e.* a full half sphere). As a matter of fact, the diffuse irradiance near the sun direction is much higher than the diffuse irradiance from directions further away from the sun. Thus, the true diffuse irradiance depends on the part of the sky observed from the pixel point of view.

Atmospheric codes that do not need a digital surface model (topography and buildings data) such as COCHISE [42] make the hypothesis that the ground is flat:  $\Theta = \Theta^o$  (the solar zenith angle),  $\delta_{dir} = 1$  (there are no shadows), and  $\Omega = 1$  (each pixel sees the entire sky). Accordingly, pixels on a slope or in shadows will have poor reflectance estimates. More precisely, if we neglect the contributions of  $I_{coup}$  and  $I_{refl}$ , we can easily derive the ratio between the estimated reflectance  $\rho$  and the true reflectance  $\rho^*$  for a given wavelength, as a function of the true local parameters  $\delta_{dir}^*$ ,  $\Theta^*$ ,  $\Omega^*$  and  $p_\Theta^*$ :

$$\frac{\rho}{\rho^*} = \frac{\delta_{dir}^* \cdot \cos \Theta^* \cdot I_{dir}^o + \Omega^* \cdot p_\Theta^* \cdot I_{dif}^o}{\cos \Theta^o \cdot I_{dir}^o + I_{dif}^o} \quad (13)$$

This ratio is the deductive bias that we introduce in the decoding part of p<sup>3</sup>VAE. It is a strong assumption on how the signal behaves under local irradiance conditions. Here we emphasize the fact that the ratio depends on the wavelength  $\lambda$  and that it is non-linear with regard to  $\delta_{dir}^*$ ,  $\cos \Theta^*$ ,  $\Omega^*$  and  $p_{\Theta}^*$ , as illustrated on Fig. 4. We argue that this behaviour could hardly be modeled by a neural network that would likely fall in local optima. We discuss the viability to neglect the coupling and the neighbouring irradiance terms in the appendix.

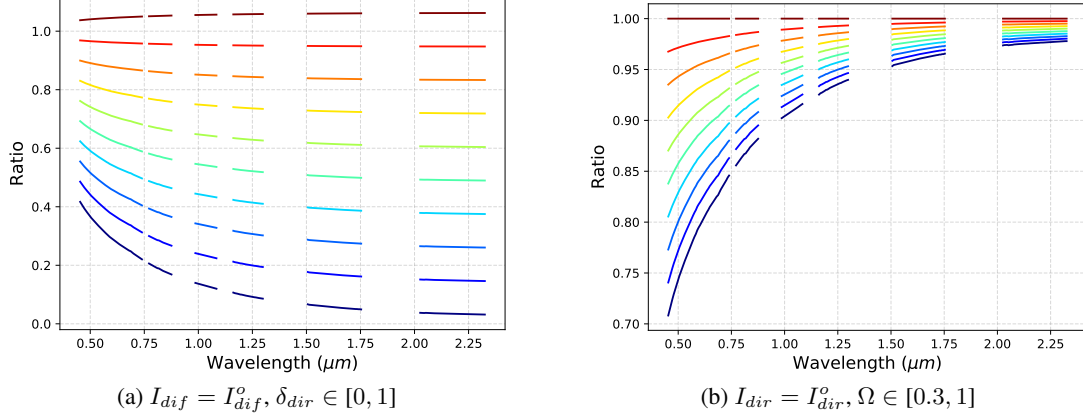


Figure 4: Ratio of the estimated reflectance under the true reflectance for varying irradiance conditions. Blue lines correspond to low values and red lines to high values of (a)  $\delta_{dir}$  and (b)  $\Omega$ .

### 3.2.2 Reflectance intrinsic inter-class variability

Reflectance intra-class variability does not only come from local irradiance conditions. One semantic land cover class gathers many different materials. For instance, a vegetation class would gather, on one hand, various tree species with different reflectance spectra, and on the other hand, individuals from the same specie with different bio-physical properties (such as water or chlorophyll content). We refer to this variability as intrinsic intra-class variability.

The key challenge of our hybrid model is to distinguish the intrinsic variability from the irradiance-based variability.

### 3.2.3 Latent variables and priors

In this section, we motivate the choice of the priors on the latent variables.

The class of a pixel is modeled by the categorical variable  $y \in \{1, \dots, C\}$ . In order to model the intrinsic and irradiance-based intra-class variabilities, we considered two latent variables,  $z_A$  and  $z_P$ , respectively. Following the radiative transfer model we derived above, we expect  $z_P$  to approximate  $\delta_{dir}$ ,  $\cos \Theta$ ,  $\Omega$  and  $p_{\Theta}$ . Although, inferring a four dimensional latent variable grounded to  $\delta_{dir}$ ,  $\cos \Theta$ ,  $\Omega$  and  $p_{\Theta}$  at the same time led to poor local optima, we constrained the latent space as follows:

$$\delta_{dir} \cos \Theta \leftarrow z_P \quad (14)$$

$$\Omega p_{\Theta} \leftarrow g(z_P) \quad (15)$$

where  $g$  is an empirical function that will be discussed in section 5.2. Since  $\delta_{dir} \in [0, 1]$  and  $\cos \Theta \in [0, 1]$ ,  $z_P$  should lie in  $[0, 1]$ . For this reason and because we would like a flexible distribution to model  $z_P$ , we chose a Beta distribution.

The latent variable  $z_A$  is not grounded to a physical quantity. However, we could interpret  $z_A$  as the different reflectance spectra one class could take (*e.g.* different tree species). Thus, we modeled  $z_A$  with a Dirichlet distribution of dimension  $n_A$  which values can be interpreted as a distribution probability or as the abundance of different subclasses.

Prior distributions are defined as follows:

$$p_{\theta}(y) := \mathcal{U}(\{1, \dots, C\}); \quad p_{\theta}(z_P) := \text{Beta}(z_P | \alpha^o, \beta^o); \quad p_{\theta}(z_A) := \text{Dir}(z_P | \gamma^o) \quad (16)$$

We empirically set  $\alpha^o$  to 1 and  $\beta^o = \frac{1 - \cos \Theta^o}{\cos \Theta^o + \epsilon} \alpha^o$  where  $\epsilon$  is a small constant to avoid division by zero and  $\Theta^o$  is the solar incidence angle. This prior distribution favors high values of  $z_P$  while  $\mathbb{E}_{p(z_P)} z_P = \cos \Theta^o$ , which is what we expect on a flat ground. We set  $\gamma^o = [1 \dots 1]_{1 \times n_A}$ , which is equivalent to having a uniform prior.

### 3.2.4 Decoder

The decoder has a physical part  $f_P$  and a statistical part  $f_A$ , parameterized by  $\theta$ .  $f_A$  estimates the true reflectance  $\hat{\rho} \in [0, 1]^B$ , where  $B$  is the spectral dimension, based on the class  $y$  and the intrinsic variability  $z_A$ :

$$\begin{aligned} f_A : \{1, \dots, C\} \times [0, 1]^{n_A} &\longrightarrow [0, 1]^B \\ (y, z_A) &\longmapsto \hat{\rho} = \sum_{k=1}^{n_A} z_A[k] f_A^1(y)[k] \end{aligned} \quad (17)$$

where  $f_A^1$  is a neural network.  $f_P$  is a deterministic function derived from the radiative transfer model described in section 3.2.1 that computes the observed reflectance  $x \in [0, 1]^B$  based on  $\hat{\rho}$  and  $z_P$ :

$$\begin{aligned} f_P : [0, 1]^B \times [0, 1] &\longrightarrow [0, 1]^B \\ (\hat{\rho}, z_P) &\longmapsto \frac{z_P I_{dir}^o + g(z_P) I_{dif}^o}{\cos \Theta^o \cdot I_{dir}^o + I_{dif}^o} \hat{\rho} \end{aligned} \quad (18)$$

In contrast with our general framework, we do not model the decoding part of the VAE with a multivariate normal. Denoting  $f_P(f_A(y, z_A), z_P)$  as  $\mu$ , we instead define the likelihood as follows:

$$p_\theta(x|y, z_P, z_A) := \frac{1}{Z} \mathcal{N}(x|\mu, \sigma^2 I) \cdot \exp\left(-\lambda \arccos\left(\frac{x^T \mu}{\|x\| \|\mu\|}\right)\right) \quad (19)$$

where  $\sigma$  and  $\lambda$  are hyperparameters and  $Z$  is a finite constant such that the density integrates to one. We demonstrate in the appendix that such a constant exists. The negative log-likelihood derives as follows:

$$-\log p_\theta(x|y, z_P, z_A) = \frac{1}{\sigma^2} MSE(x, \mu) + \lambda \arccos\left(\frac{x^T \mu}{\|x\| \|\mu\|}\right) + C \quad (20)$$

where  $C$  is a constant. Therefore, maximising the likelihood of the data is equivalent to minimising a linear combination of the mean squared error and the spectral angle between the observations  $x^{(i)}$  and  $\mu^{(i)} = f_P(f_A(y^{(i)}, z_A^{(i)}), z_P^{(i)})$ . The other consequence of this additional term in the density is that, without knowing the value of the constant  $Z$ , we cannot properly evaluate the likelihood for a given data point and neither sample from the likelihood. However, it is not an issue in our case because we are only interested in the predictions of the model.

### 3.2.5 Encoder

The approximated posterior (parameterized by  $\phi$ ), *i.e.* the encoding part, is defined as follows:

$$q_\phi(z_P, z_A|x, y) := q_\phi(z_P|x, y) q_\phi(z_A|x, y) \quad (21)$$

$$q_\phi(z_P|x, y) := \text{Beta}(z_P|\alpha(x, y), \beta(x, y)); \quad q_\phi(z_A|x, y) := \text{Dir}(z_A|\gamma(x, y)) \quad (22)$$

$\alpha$ ,  $\beta$  and  $\gamma$  are neural networks that will be described in details in section 5.

## 4 Data

In this section, we describe the data used in our experiments. We simulated an airborne hyperspectral image with the radiative transfer software DART [44]. 300 spectral bands with a 6.5nm resolution and a 0.5m ground sampling distance were simulated, without simulating the Earth-atmosphere coupling. A false-color image and its ground truth are shown in Fig. 5. The scene was simulated with five materials (vegetation, sheet metal, sandy loam, tile and asphalt) whose mean reflectance spectra are shown in fig. 6 (spectra were sampled with a gaussian noise). Some classes gather different materials to have a realistic intrinsic inter-class variability. For instance, the vegetation class has three spectra which correspond to healthy grass, stressed grass and eucalyptus reflectances. We refer to those different materials within one class as subclasses. The azimuth angle is equal to 180 degrees, the solar zenithal angle is equal to 30 degrees and the roofs have different slopes. Moreover, to reproduce the scarcity of annotations in remote sensing, we labeled only a few pixels in the training data set and used the unlabeled pixels in our validation set. In particular, the training data set:

- does not include vegetation, asphalt and sandy loam pixels in the shadows,



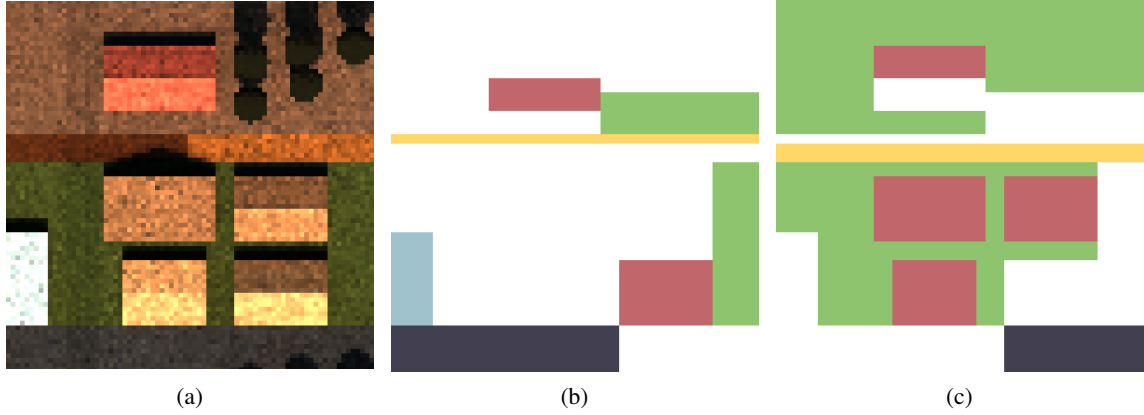


Figure 5: (a) False color composition of the simulated hyperspectral image and its (b) training and (c) validation ground truths.

- partially includes tile pixels on different slopes,
- contains all pixels of sheet metal.

Simulating a scene was very convenient as we precisely knew the topography and the reflectance of each material. To test our model, we computed roughly 10,000 test spectra per class with different slopes, direct irradiance and sky viewing angle. We also made different combinations of reflectance spectra within each class. Precisely, the factors that were used to generate a spectra  $x$  were the class  $y$ , the portion of direct irradiance  $\delta_{dir}$ , the solar incidence angle  $\Theta$ , the sky viewing angle factor  $\Omega$ , the anisotropy correction coefficient  $p_{\Theta}$ , the intra-class mixing coefficient  $\alpha \in [0, 1]$  and the subclass configuration  $\eta$ :

$$x = \frac{\delta_{dir} \cos \Theta I_{dir}^o + \Omega p_{\Theta} I_{dif}^o}{\cos \Theta \cdot I_{dir}^o + I_{dif}^o} \tilde{\rho} \quad \text{with} \quad \tilde{\rho} = \alpha \rho[y][\eta_1] + (1 - \alpha) \rho[y][\eta_2] \quad (23)$$

where  $\rho[y][\eta_i]$  denotes the reflectance spectrum of the  $\eta_i$ th subclass of class  $y$ .

Simulating individual test spectra was very convenient to analyze the results, as we will see in section 5. However, as we have seen in section 3.2, neighbouring pixels contribute to the observed reflectance spectrum. Thus, our test data set does not account neither for the Earth-atmosphere coupling contribution nor the neighbouring contribution. Therefore, we simulated additional scenes and conducted more experiments that are described and discussed in the appendix.

## 5 Experiments

We compared our model, p<sup>3</sup>VAE, with a conventional CNN (Convolutional Neural Network), a conventional gaussian VAE and a physics-guided VAE. Models are optimized and tested on the data sets described in section 4. In this section, we broadly present the architecture of the models (although exhaustive details are in the appendix), present the optimization details, the metrics and the results.

### 5.1 Models architectures

**p<sup>3</sup>VAE.** As we have seen in section 3.2, the parameters of the posterior distributions  $q_{\phi}(z_P|x, y)$  and  $q_{\phi}(z_A|x, y)$  are computed with neural networks  $\alpha$ ,  $\beta$  and  $\gamma$ .  $\alpha$  and  $\beta$  are dense neural networks because we believe that  $z_P$  can be inferred only with affine transformations of  $x$  and  $y$ . As far as  $z_A$  is more related to the shape of  $x$ , we found more relevant to model  $\gamma$  by a convolutional neural network. Concerning the decoder,  $f_A^1$  is the element-wise multiplication of two  $B \times n_A$  matrices computed with dense neural networks. The approximate predictive distribution  $q_{\phi}(y|x)$  is computed with a convolutional neural network that has rigorously the same architecture than the CNN model described below. The model is trained using gradient stopping as described in section 3.1.2.

**CNN.** The CNN architecture is very similar to conventional CNNs used in the hyperspectral literature [45]. It is composed of two spectral convolutions (with one kernel per continuous spectral domain), a skip connection and a max-pooling layer, followed by fully connected layers.

**Gaussian VAE.** The encoder of the gaussian VAE uses the same convolutional neural network used in the encoder of p<sup>3</sup>VAE. The dimension of the latent variable  $z$  is equal to  $\dim(z_A) + \dim(z_P)$ . The decoder is composed of dense layers and a final sigmoid activation.

**Physics-guided VAE.** In order to compare the benefits of the physics model only, we designed a physics-guided VAE which encoder and decoder have the same architectures that the ones of p<sup>3</sup>VAE. The only difference is that the decoder has only a machine learning part  $f_A$ . The model is trained using gradient stopping as described in section 3.1.2.

Every classifiers are turned into bayesian classifiers using MC Dropout [46].

## 5.2 Optimization

Every models are optimized with the Adam stochastic descent gradient algorithm [47] for 100 epochs and a batch size of 64. We tuned the learning rate between  $5 \cdot 10^{-5}$  and  $1 \cdot 10^{-4}$  to reach loss convergence on the training and validation sets. We modeled the empirical function  $g : z_P \mapsto \Omega p_\Theta$  by an affine transformation and tuned its parameters on the validation set. We retained  $g(z_P) = z_P + 0.2$ , which led to good spectral reconstruction under low direct irradiance conditions despite being very simplistic. We weighted the Kullback-Leibler divergence term in equations (4) and (5) by  $\beta = 10^{-4}$  following [11] technique. We also weighted the entropy term in equation (5) to balance between high accuracy and high uncertainty with a  $10^{-1}$  coefficient. Besides, we applied a Ridge regularization on the weights of the classifiers and encoders with a  $10^{-2}$  penalty coefficient.

## 5.3 Metrics

We computed the widely used F1 score for each class, which reflects the performance of the models on the segmentation task, as well as the JEMMIG metric that measures disentanglement. A latent space is said to be disentangled if its variables independently capture true underlying factors that explain the data [48]. Assessing whether a representation is disentangled is still an active research topic. Nevertheless, [48] made a review of state-of-the art metrics to measure disentanglement, that they decompose in modularity, compactness and explicitness. **Modularity** guarantees that a variation in one factor only affects a subspace of the latent space, and that this subspace is only affected by one factor. **Compactness** relates to the size of the subspace affected by the variation in one factor. Finally, **explicitness** expresses how explicit is the relation between the latent code and the factors. [48] compared thirteen disentanglement metrics, from which we chose the JEMMIG (Joint Entropy Minus Mutual Information Gap) metric [49] because it measures modularity, compactness and explicitness at the same time, and relies on few hyper-parameters.

The JEMMIG metric is computed based on a data set of factors (e.g. categorical classes, local irradiance conditions, etc. described in section 4) and latent codes (the latent representation inferred by the generative models based on the reflectance spectra generated from the factors). In the following, we denote  $v$  as the factors and  $z$  as the latent code. JEMMIG estimates the mutual information between factors and latent codes. It enhances the MIG (Mutual Information Gap) metric [50]. Intuitively, the mutual information  $I(v, z)$  between  $v$  and  $z$  indicates how much information we have about  $z$  when we know  $v$ . Therefore, the mutual information between a factor  $v_i$  (e.g.  $\delta_{dir} \cos \Theta$ ) and its related subspace  $z_K$  (e.g.  $z_P$ ) should be high while the mutual information between  $v_i$  and other subspaces should be low. JEMMIG computes the mutual information between each code and factor  $I(v_i, z_j)$  and retains the two latent variables  $z_*$  and  $z_o$  with the highest mutual information  $I(v_i, z_*)$  and  $I(v_i, z_o)$ . The difference between  $I(v_i, z_*)$  and  $I(v_i, z_o)$  reflects how much information related to the factor  $v_i$  is expressed by  $z_*$  only. Conversely,  $z_*$  could contain information about other factors than  $v_i$ . Thus, to account for the modularity property, JEMMIG also computes the joint entropy  $H(v_i, z_*)$  between  $v_i$  and  $z_*$ , resulting in the following metric:

$$JEMMIG := H(v_i, z_*) - (I(v_i, z_*) - I(v_i, z_o)) \quad (24)$$

We report the joint entropy and the mutual information gap individually, since, on the one hand, they measure two different properties, and on the other hand, they scale differently. In addition, we report a normalized version of the JEMMIG metric introduced in [48] that scales between 0 and 1, the higher being the better.

## 5.4 Results

### 5.4.1 Accuracy metrics

**F1 score.** Mean F1 score per class over 10 runs is showed on table 1. First, all semi-supervised models outperformed the fully supervised CNN in terms of average F1 score by a margin of at least 4%. Second, using  $q_\phi(y|x)$  to make the predictions, semi-supervised models had small differences in term of F1 score. Third, making predictions using  $\arg \max_y p_\theta(y|x)$ , large gains were obtained with the gaussian VAE and p<sup>3</sup>VAE over the conventional CNN. In particular, p<sup>3</sup>VAE made significant improvements over the gaussian VAE (+3%), the physics-guided VAE (+9%) and

Table 1: Mean F1 score per class over 10 runs

| Inference model    |   | Classes     |             |             |             |             | Average     |
|--------------------|---|-------------|-------------|-------------|-------------|-------------|-------------|
|                    |   | Vegetation  | Sheet metal | Sandy loam  | Tile        | Asphalt     |             |
| CNN                | $q_\phi(y x)$                                 | 0.90        | 0.81        | 0.77        | 0.79        | 0.75        | 0.80        |
|                    | $q_\phi(y x)$ (full annotations) <sup>1</sup> | 0.92        | 0.79        | <b>0.90</b> | 0.87        | 0.86        | 0.86        |
| Gaussian VAE       | $q_\phi(y x)$                                 | 0.93        | 0.80        | 0.87        | 0.86        | 0.74        | 0.84        |
|                    | $\arg \max_y p_\theta(y x)$                   | 0.94        | 0.88        | <b>0.90</b> | <b>0.92</b> | 0.85        | 0.90        |
| Physics-guided VAE | $q_\phi(y x)$                                 | 0.93        | 0.81        | 0.86        | 0.86        | 0.76        | 0.84        |
|                    | $\arg \max_y p_\theta(y x)$                   | 0.86        | 0.85        | 0.83        | 0.75        | 0.77        | 0.81        |
| p <sup>3</sup> VAE | $q_\phi(y x)$                                 | 0.92        | 0.82        | 0.88        | 0.87        | 0.81        | 0.86        |
|                    | $\arg \max_y p_\theta(y x)$                   | <b>0.96</b> | <b>0.97</b> | <b>0.90</b> | 0.90        | <b>0.93</b> | <b>0.93</b> |

<sup>a</sup>The CNN was optimized with every pixels labeled on the image (*i.e.* the labeled and unlabeled sets showed on Fig. 5), in contrast with every other cases where the image is partially labeled.

the CNN (+13%). A statistical hypothesis test shows that the average F1 score of the gaussian VAE and p<sup>3</sup>VAE are significantly different: we reject the hypothesis of equal average with a 0.3% p-value. Even with exhaustive annotations (we added the labels of the "unlabeled" pixels in the training data set and we refer to this setting as *full annotations* in table 1), p<sup>3</sup>VAE outperformed the CNN by a 7% margin. Besides, we can notice that the accuracy for *Sheet metal*, which is the only class with homogeneous irradiance on the training image, is barely the same for every models when  $q_\phi(y|x)$  is used. Except for the physics-guided VAE, better predictions were made when computing  $\arg \max_y p_\theta(y|x)$ .

**Local irradiance estimate.** Fig. 6 shows, for each class, the inferred  $z_P$  by p<sup>3</sup>VAE against the true  $\delta_{dir} \cos \Theta$  of the test data set. Correctly classified pixels are shown as purple points while wrongly predicted pixels are shown as orange points. The size of the points is proportional to the exponential of the empirical standard deviation of  $z_P$ . First, we notice that most confusions are made when  $\delta_{dir} \cos \Theta$  is poorly estimated or when its true value is low. Secondly, we see that most confusions go hand in hand with high  $z_P$  uncertainty estimates, meaning that two classes are likely, but under very different irradiance conditions. Finally, we see that there is a bias, in the sense that the average prediction of  $\delta_{dir} \cos \Theta$  is different from its true value.  $\delta_{dir} \cos \Theta$  is mostly under-estimated, which is the counterpart of over-estimated reflectance spectra as shown in Fig. 6 and commented below.

**Estimated reflectance.** Fig. 6 shows the estimated reflectance spectra by p<sup>3</sup>VAE. There are four estimated spectra per class as we set  $n_A = 4$  in our experiments. p<sup>3</sup>VAE rather well estimated the shape of the spectra. For instance, the absorption peak of clay at 2.2 $\mu$ m is reconstructed by p<sup>3</sup>VAE for the classes Tile and Sandy loam. However, the intensity of the spectra is not accurate, which is a consequence of the bias in the  $\delta_{dir} \cos \Theta$  prediction. Finally, we highlight that p<sup>3</sup>VAE inferred realistic reflectance spectra whereas the estimated spectra by the physics-guided VAE look like white noise (see Fig. 10 in the appendix).

#### 5.4.2 Disentanglement

Table 2 shows the averaged JEMMIG metric for each factor over 10 runs.  $y$  is the class of the pixel,  $\delta_{dir} \cos \Theta$  and  $\Omega p_\Theta$  are the local irradiance conditions,  $\alpha$  is the intra-class mixing coefficient and  $\eta$  represents the subclasses configuration (see section 4 for more details). Better values of the normalized JEMMIG score were obtained with the physics-guided VAE except for the class factor, which had its largest value with p<sup>3</sup>VAE. Same observations can be drawn concerning the joint entropy term. In contrast, p<sup>3</sup>VAE led to higher (*i.e.* better) mutual information gaps for every factors except for the  $\Omega p_\Theta$  factor. Largest discrepancies in term of disentanglement performance are observed for the mutual information gap (MIG) for the irradiance conditions factors. As a matter of fact, the MIG for  $\delta_{dir} \cos \Theta$  was 12 times higher with p<sup>3</sup>VAE than with the physics-guided VAE while the MIG for  $\Omega p_\Theta$  was 8 times higher with the gaussian VAE than with p<sup>3</sup>VAE.

**Maximum likelihood estimates.** A qualitative way to evaluate the disentanglement of the latent space is to plot spectra that maximize the generative model likelihood for different values of the latent variables. Fig. 7 shows the maximum likelihood estimates of the class tile for the physics-guided VAE and p<sup>3</sup>VAE. The different estimates were obtained by interpolating within the latent space.

We see on Fig. 7 that latent variables  $z_P$  and  $z_A$  are disentangled by p<sup>3</sup>VAE. Firstly, for a given column, the variations of the spectra are only induced by the variation in irradiance conditions : the shape roughly stays the same but the intensity changes. Secondly, for a given row, the variations of the spectra are only induced by the change in the nature of matter : the intensity is the same but the shape changes.

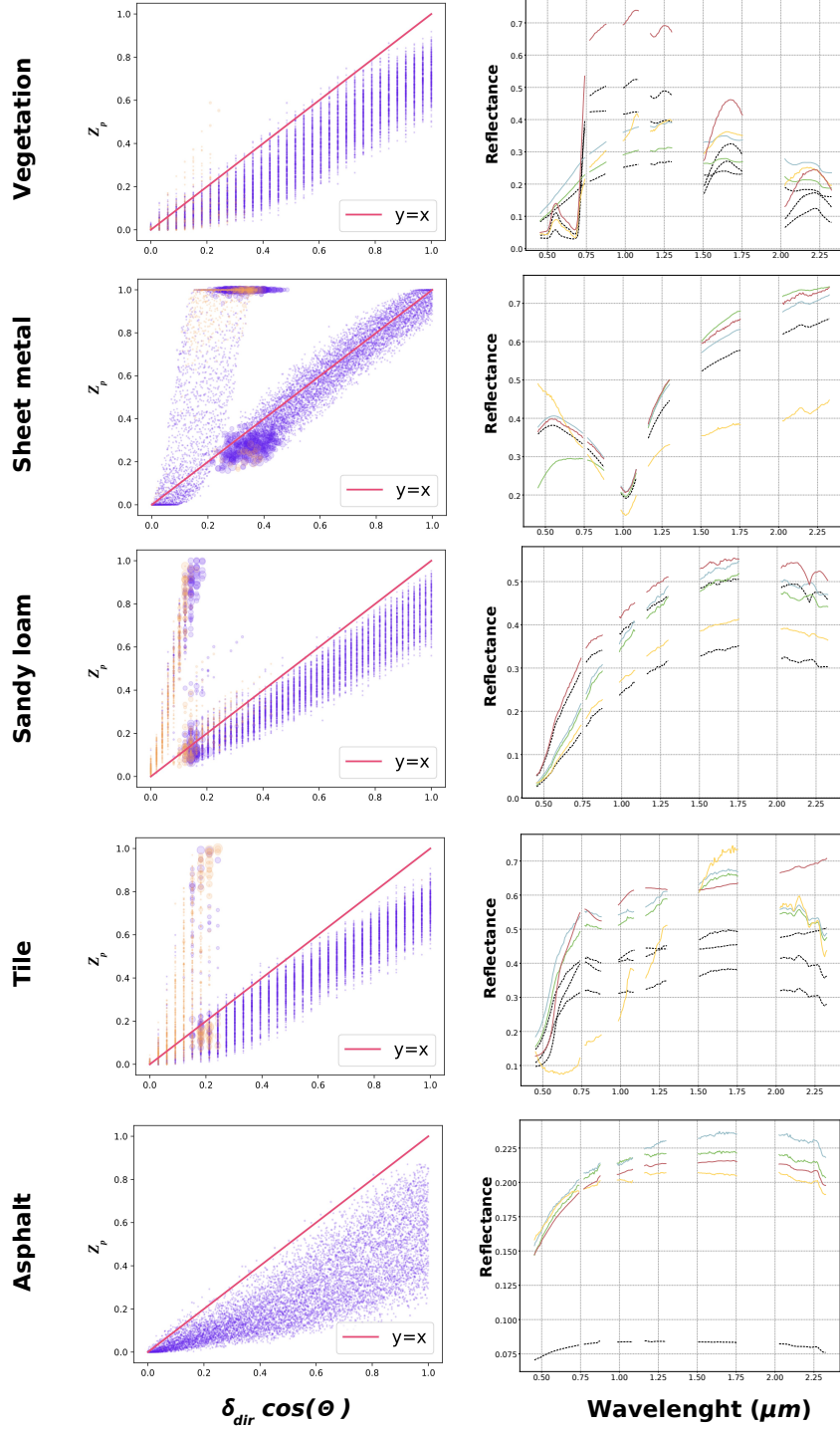


Figure 6: **On the left column:** predicted  $z_P$  against true  $\delta_{dir} \cos \Theta$  for each class with p<sup>3</sup>VAE. Each point represents a pixel, which is correctly classified if shown in purple, or wrongly classified if shown in orange. The size of the points is proportional to the exponential of the empirical standard deviation of  $z_P$ . **On the right column:** Estimated class reflectance for each class with p<sup>3</sup>VAE. True reflectance spectra, that were used for data simulation, are plotted in dashed black lines.

In contrast, the physics-guided VAE does not disentangle the latent variables. A variation along one latent variables induces a change both in the irradiance conditions and on the type of tile.

Table 2: Mean JEMMIG metric over 10 runs

| Metric  | Model              | Factors     |                            |                     |             |             | Average     |
|---|--------------------|-------------|----------------------------|---------------------|-------------|-------------|-------------|
|   |                    | Class       | $\delta_{dir} \cos \Theta$ | $\Omega p_{\Theta}$ | $\alpha$    | $\eta$      |             |
| Joint entropy ( $\downarrow$ ) <sup>1</sup>         | Gaussian VAE       | 2.8         | 6.9                        | 6.9                 | 4.5         | 4.5         | 5.1         |
|   | Physics-guided VAE | 3.1         | <b>6.4</b>                 | <b>6.0</b>          | <b>4.4</b>  | <b>4.4</b>  | <b>4.7</b>  |
|   | p <sup>3</sup> VAE | <b>2.68</b> | 7.3                        | 7.2                 | <b>4.4</b>  | <b>4.4</b>  | 5.2         |
| Mutual information gap ( $\uparrow$ ) <sup>1</sup>  | Gaussian VAE       | 0.62        | 0.18                       | <b>0.096</b>        | 0.20        | 0.20        | 0.26        |
|   | Physics-guided VAE | 1.0         | 0.068                      | 0.021               | 0.28        | 0.28        | 0.33        |
|   | p <sup>3</sup> VAE | <b>1.2</b>  | <b>0.85</b>                | 0.012               | <b>0.31</b> | <b>0.31</b> | <b>0.54</b> |
| Normalized JEMMIG score ( $\uparrow$ ) <sup>1</sup> | Gaussian VAE       | 0.67        | 0.22                       | 0.12                | 0.39        | 0.39        | 0.36        |
|   | Physics-guided VAE | 0.69        | <b>0.26</b>                | <b>0.21</b>         | <b>0.42</b> | <b>0.42</b> | <b>0.40</b> |
|   | p <sup>3</sup> VAE | <b>0.78</b> | 0.25                       | 0.061               | <b>0.42</b> | <b>0.42</b> | 0.38        |

<sup>a</sup>( $\downarrow$ ) means that the lower is the better while ( $\uparrow$ ) means that the higher is the better.

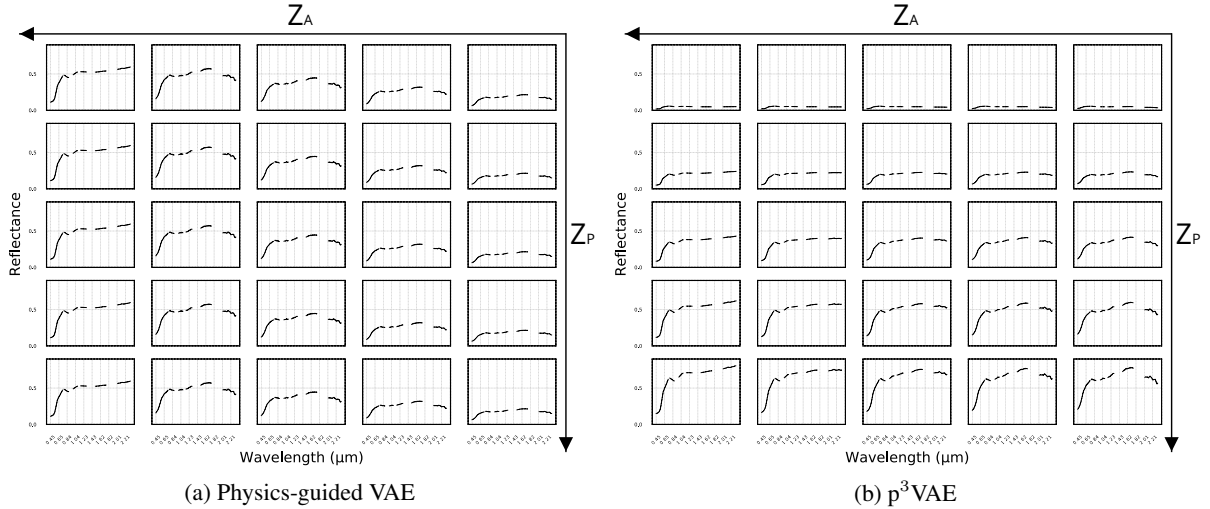


Figure 7: Maximum likelihood estimates of the learned generative models along  $z_P$  (on the y-axis) and  $z_A$  (on the x-axis).  $z_P$  is interpolated between its minimum (top row) and maximum (bottom row) values inferred on the training data set.  $z_A$  is interpolated between two samples taken from two different types of tile (left and right columns), inferred on the training data set.

## 5.5 Ablation study

In this section, we study the impact of gradient stopping (described in section 3) on the optimization of p<sup>3</sup>VAE. Table 3 shows the average F1 score of p<sup>3</sup>VAE optimized with or without gradient stopping. Statistical hypothesis tests show that gradient stopping has not a significant influence on the model performance, for both inference techniques. However, a look at the estimated reflectance spectra by p<sup>3</sup>VAE without gradient stopping shows that the machine learning part learns unrealistic spectra. For instance, we plot the estimated reflectance spectra of the class asphalt by p<sup>3</sup>VAE without gradient stopping on Fig. 8. Among the four estimated spectra, one is actually similar to a real asphalt spectrum, one is similar to a vegetation spectrum and others do not correspond to any material in the scene.

## 6 Discussion

In this section, we discuss the performances of p<sup>3</sup>VAE, the particularities of its optimization and its relation to  $\phi$ -VAE. Because our experiments showed that its interpolation capabilities are similar to conventional generative models, we focus on its extrapolation and disentanglement capacities which are greatly increased by its physical part.

Table 3: p<sup>3</sup>VAE average F1 score

| Inference technique         | no gs <sup>1</sup> | gs <sup>1</sup> |
|-----------------------------|--------------------|-----------------|
| $q_\phi(y x)$               | 0.86               | 0.86            |
| $\arg \max_y p_\theta(y x)$ | 0.92               | 0.93            |

<sup>1</sup>gs refers to the gradient stopping technique described in section 3

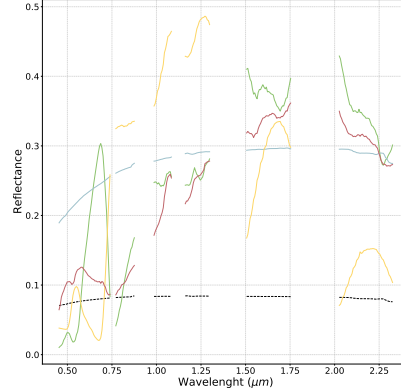


Figure 8: Estimated reflectance spectra of the class asphalt by p<sup>3</sup>VAE without gradient stopping

## 6.1 Extrapolation capabilities

p<sup>3</sup>VAE demonstrated high extrapolation capabilities in our experiments, especially when predictions were made by computing  $\arg \max_y p(y|x)$  (as described in section 3.1.3). As a matter of fact, the physics part  $f_P$  is explicitly used in this case. In contrast, the physics model is only used during optimization when we perform inference with the predictive distribution  $q_\phi(y|x)$ , which yields less robust predictions. In our experiments, the test data set is generated with out-of-distribution physical factors, *i.e.* test irradiance conditions out of the range of the training irradiance conditions. In particular, the pixels of sheet metal (both labeled and unlabeled) are only seen under the same irradiance conditions during training. For this reason, the CNN and the conventional semi-supervised models failed to predict sheet metal pixels under roughly 20% of the test irradiance conditions using the predictive distribution. However, predictions from the gaussian VAE using  $\arg \max_y p(y|x)$  approximately reduced by half the confusions over the sheet metal class. Besides, the CNN with exhaustive annotations was still worse than gaussian VAE and p<sup>3</sup>VAE. This illustrates that generative models as a whole can truly grasp some factors of variation that generalize to out-of-distribution data, in contrast to the predictive distribution only. In particular, the physics part of p<sup>3</sup>VAE highly increased the extrapolation performances for classes with little inter-class similarities (*e.g.* only 3% of mistakes for the sheet metal class), since the physics model can extrapolate by nature. The limits of p<sup>3</sup>VAE are reached when two spectra intrinsically share spectral features, such as tile and sandy loam: the model has similar or slightly smaller accuracy, but higher and more meaningful uncertainty, as discussed below. Furthermore, the physics-guided VAE made worse predictions with  $\arg \max_y p(y|x)$  than with the predictive distribution. We provide an explanation through the analysis of the JEMMIG metric in the next subsection.

We can derive an uncertainty estimate  $\sigma(z_P)$  over  $\delta_{dir} \cos \Theta$  from p<sup>3</sup>VAE, which yields easily explainable predictions. In other words, p<sup>3</sup>VAE can tell us that different classes are likely, but under different conditions. Uncertainty estimates over latent variables grounded to physical properties are naturally more explainable than uncertainty estimates over abstract variables. From a user perspective, this is a valuable feature. Besides, the entropy of the predictive distribution  $H(q_\phi(y|x))$  gives a complementary uncertainty estimate. In fact,  $H(q_\phi(y|x))$  and  $\sigma(z_P)$  poorly correlate ( $R^2 \approx 0.2$  in our experiments), because the classifier is generally uncertain in the shadows although  $z_P$  is well inferred.

## 6.2 Disentanglement

We evaluated the disentanglement of the latent space qualitatively and quantitatively. A major difference that we should highlight is that the quantitative approach evaluates how a variation of the factors induces a variation of the latent code. The qualitative approach on the other hand evaluates how a change in the latent code induces a change in the observation. Therefore, assessing the disentanglement qualitatively requires expert knowledge.

Qualitatively, p<sup>3</sup>VAE showed higher disentanglement capabilities than other generative models. The decoder architecture, with the machine learning part and the physical part, naturally induces a disentanglement of the latent space. Generated samples with varying  $z_P$  values automatically yield physically meaningful variations of spectra. Quantitatively, the JEMMIG metric highlights the rough approximation of the true diffuse irradiance as far as p<sup>3</sup>VAE estimates the same  $\Omega p_\Theta$  given a  $\delta_{dir} \cos \Theta$  estimate: this is the reason why the mutual information gap is very low for the diffuse irradiance factor  $\Omega p_\Theta$ . In contrast, the mutual information gap for the direct irradiance factor is very high,

which highlights the natural disentanglement induced by the physics model which grounds  $z_P$  to  $\delta_{dir} \cos \Theta$ . We believe that the joint entropy term for the direct irradiance factor is large because the bias between the predicted  $z_P$  and the true  $\delta_{dir} \cos \Theta$  depends on the class, which leads to an unclear relation between the factor and the code when the class  $y$  is not known. Concerning the physics-guided VAE, it suffered from mode collapse during our experiments. The very low mutual information gap for  $\delta_{dir} \cos \Theta$  shows that the physics-guided VAE failed to capture this factor of variation. As a consequence, the model predicts approximately the same  $\delta_{dir} \cos \Theta$  for any spectrum. This is why it had mediocre performances using  $\arg \max_y p(y|x)$  compared to other generative models. This also explains why the physics-guided VAE had rather low joint entropies for the irradiance factors. Thus, in the case of mode collapse, the JEMMIG metric can be misleading and we argue that the mutual information gap is more relevant in this case.

### 6.3 Optimization

**Loss landscape.** In our experiments, we had more trouble to reach convergence with p<sup>3</sup>VAE than other models. In particular, the training loss for some configurations of weights at initialization systematically diverged, irrespective to the learning rate. We guess that the physics model implicitly constrains the admissible solutions of the machine learning part, which leaves the optimization in a local minima from the beginning, for some specific weight initialization.

**Gradient stopping.** The ablation study described in 4 showed that gradient stopping has no significant impacts on the performances of p<sup>3</sup>VAE but constrain the neural networks to learn realistic relations between the class labels and the estimated reflectance spectra. Because some values of  $(y, z_A, z_P)$  can lead to good reconstructions even with very bad reflectance estimates, the performance metrics are not impacted. As a matter of fact,  $z_A$  and  $z_P$  given  $x$  and  $y$  are correlated. In particular, unrealistic spectra go hand in hand with very low direct irradiance. Without gradient stopping however, p<sup>3</sup>VAE loses physical sense and interpretability.

### 6.4 Relation to physics-integrated VAEs ( $\phi$ -VAE)

Physics-integrated VAEs [2] are, to our knowledge, the first general framework that combines physics models and machine learning models in a variational autoencoder. Our model falls in their formalism as far as  $\phi$ -VAE latent space is partitioned into two types of data,  $z_A$  and  $z_P$  which are inputs of a machine learning model  $f_A$  and of a physics model  $f_P$ . The differences between  $\phi$ -VAE and our model, though, are twofold.

**Unsupervised VS semi-supervised setting.** The first difference, which is minor in architecture, but significant in optimization, is that the latent variables of  $\phi$ -VAE are never observed. In contrast, we partially observe the discrete variable  $y$  of our model during optimization, as we discussed in section 3.1.2.

**Imperfect VS perfect physics model.** There is a major difference of philosophy between  $\phi$ -VAE and p<sup>3</sup>VAE.  $\phi$ -VAE tackles problems for which an imperfect physics model can approximate the data distribution. In this context, the machine learning part  $f_A$  of  $\phi$ -VAE models the residual error of its imperfect physics model  $f_P$ . Intuitively,  $z_A$  *explains* the part of the observation  $x$  that was not *explained* by  $z_P$ . This has two practical consequences:

- Firstly, the latent variable  $z_P$  and  $z_A$  of  $\phi$ -VAE are dependent conditioned on  $x$ :

$$q_\phi(z_A, z_P|x) := q_\phi(z_A|x)q_\phi(z_P|x, z_A) \quad (25)$$

In contrast, we assume that  $z_A$  and  $z_P$  are independent conditioned on  $x$  and  $y$ .

- Secondly, the expectation of the likelihood  $p_\theta(x|z_A, z_P)$  of  $\phi$ -VAE is defined as follows:

$$p_\theta(x|z_P, z_A) := \mathcal{N}(x|\mathcal{F}[f_A, f_P; z_P, z_A], \Sigma) \quad (26)$$

where  $\mathcal{F}$  is a functional that evaluates  $f_A \circ f_P$  or solves an equation in the form  $f_A \circ f_P = 0$ . The notable difference is that the machine learning model of  $\phi$ -VAE is a function of the physics model output, which is the opposite for our model.

Because the physics part of  $\phi$ -VAE is imperfect, a specific regularization technique is necessary to control the representation power of the machine learning part. In contrast, our experiments showed that neural networks in p<sup>3</sup>VAE cannot really impinge the physics model because they control different subspaces of the latent code.

## 7 Conclusion

We introduced p<sup>3</sup>VAE, a hybrid generative model that combines conventional neural networks with a physics model. In this framework, the perfect physical part partially explains the true underlying factors of data variation, which naturally leads to a disentangled latent space and to high extrapolation capabilities. The semi-supervised optimization

of p<sup>3</sup>VAE led to a good use of the machine learning part, which was reflected with physically meaningful inferred latent variables and uncertainty estimates. Finally, the introduced inference technique fully leveraged the physical model and empirically demonstrated its benefits on a simulated remote sensing scene, in comparison with conventional semi-supervised generative models and supervised convolutional neural networks. In future work, we would like to apply p<sup>3</sup>VAE to real Earth observation data, with higher complexity and intrinsic intra-class variability.

**Acknowledgments.** We thank Pr. Jean Philippe Gastellu-Etchegorry for his precious help handling the DART [44] software.

## References

- [1] Maziar Raissi, Paris Perdikaris, and George E Karniadakis. Physics-informed neural networks: A deep learning framework for solving forward and inverse problems involving nonlinear partial differential equations. *Journal of Computational physics*, 378:686–707, 2019.
- [2] Naoya Takeishi and Alexandros Kalousis. Physics-integrated variational autoencoders for robust and interpretable generative modeling. *Advances in Neural Information Processing Systems*, 34:14809–14821, 2021.
- [3] Tom M Mitchell. *The need for biases in learning generalizations*. Department of Computer Science, Laboratory for Computer Science Research . . . , 1980.
- [4] Shengjia Zhao, Hongyu Ren, Arianna Yuan, Jiaming Song, Noah Goodman, and Stefano Ermon. Bias and generalization in deep generative models: An empirical study. *Advances in Neural Information Processing Systems*, 31, 2018.
- [5] Laura von Rueden, Sebastian Mayer, Katharina Beckh, Bogdan Georgiev, Sven Giesselbach, Raoul Heese, Birgit Kirsch, Michal Walczak, Julius Pfrommer, Annika Pick, et al. Informed machine learning-a taxonomy and survey of integrating prior knowledge into learning systems. *IEEE Transactions on Knowledge & Data Engineering*, (01):1–1, 2021.
- [6] Christian Jacobsen and Karthik Duraisamy. Disentangling generative factors of physical fields using variational autoencoders. *arXiv preprint arXiv:2109.07399*, 2021.
- [7] C Wei, J Zhang, and Chenglin Wu. Thermodynamic consistent neural networks for learning material interfacial mechanics. In *NeurIP workshop*, 2020.
- [8] Nathaniel Trask, Carianne Martinez, Kookjin Lee, and Brad Boyce. Unsupervised physics-informed disentanglement of multimodal data for high-throughput scientific discovery. *arXiv preprint arXiv:2202.03242*, 2022.
- [9] Diederik P Kingma and Max Welling. Auto-encoding variational bayes. *stat*, 1050:1, 2014.
- [10] Irina Higgins, Loic Matthey, Xavier Glorot, Arka Pal, Benigno Uria, Charles Blundell, Shakir Mohamed, and Alexander Lerchner. Early visual concept learning with unsupervised deep learning. *stat*, 1050:20, 2016.
- [11] Irina Higgins, Loic Matthey, Arka Pal, Christopher Burgess, Xavier Glorot, Matthew Botvinick, Shakir Mohamed, and Alexander Lerchner. beta-vae: Learning basic visual concepts with a constrained variational framework. 2016.
- [12] Mikhail Figurnov, Shakir Mohamed, and Andriy Mnih. Implicit reparameterization gradients. *Advances in neural information processing systems*, 31, 2018.
- [13] Weonyoung Joo, Wonsung Lee, Sungrae Park, and Il-Chul Moon. Dirichlet variational autoencoder. *Pattern Recognition*, 107:107514, 2020.
- [14] Yijun Xiao, Tiancheng Zhao, and William Yang Wang. Dirichlet variational autoencoder for text modeling. *arXiv preprint arXiv:1811.00135*, 2018.
- [15] Emilien Dupont. Learning disentangled joint continuous and discrete representations. *Advances in Neural Information Processing Systems*, 31, 2018.
- [16] Miguel A Aragon-Calvo and JC Carvajal. Self-supervised learning with physics-aware neural networks–i. galaxy model fitting. *Monthly Notices of the Royal Astronomical Society*, 498(3):3713–3719, 2020.
- [17] Andrei Stoian, Vincent Poulain, Jordi Inglada, Victor Poughon, and Dawa Derksen. Land cover maps production with high resolution satellite image time series and convolutional neural networks: Adaptations and limits for operational systems. *Remote Sensing*, 11(17):1986, 2019.
- [18] Chacha Chen, Guanjie Zheng, Hua Wei, and Zhenhui Li. Physics-informed generative adversarial networks for sequence generation with limited data. In *NeurIPS Workshop on Interpretable Inductive Biases and Physically Structured Learning*, 2020.



- [19] Sifan Wang, Yujun Teng, and Paris Perdikaris. Understanding and mitigating gradient flow pathologies in physics-informed neural networks. *SIAM Journal on Scientific Computing*, 43(5):A3055–A3081, 2021.
- [20] Cagatay Yildiz, Markus Heinonen, and Harri Lahdesmaki. Ode2vae: Deep generative second order odes with bayesian neural networks. *Advances in Neural Information Processing Systems*, 32, 2019.
- [21] Ori Linial, Neta Ravid, Danny Eytan, and Uri Shalit. Generative ode modeling with known unknowns. In *Proceedings of the Conference on Health, Inference, and Learning*, pages 79–94, 2021.
- [22] Tejas D Kulkarni, William F Whitney, Pushmeet Kohli, and Josh Tenenbaum. Deep convolutional inverse graphics network. *Advances in neural information processing systems*, 28, 2015.
- [23] Zheng Ding, Yifan Xu, Weijian Xu, Gaurav Parmar, Yang Yang, Max Welling, and Zhuowen Tu. Guided variational autoencoder for disentanglement learning. In *Proceedings of the IEEE/CVF Conference on Computer Vision and Pattern Recognition*, pages 7920–7929, 2020.
- [24] Elliott Gordon Rodriguez. On disentanglement and mutual information in semi-supervised variational auto-encoders. In *Proceedings of the IEEE/CVF Conference on Computer Vision and Pattern Recognition*, pages 1257–1262, 2021.
- [25] Ricky TQ Chen, Xuechen Li, Roger B Grosse, and David K Duvenaud. Isolating sources of disentanglement in variational autoencoders. *Advances in neural information processing systems*, 31, 2018.
- [26] Yann LeCun and Corinna Cortes. MNIST handwritten digit database. 2010.
- [27] Jesper E Van Engelen and Holger H Hoos. A survey on semi-supervised learning. *Machine Learning*, 109(2):373–440, 2020.
- [28] Isaac Triguero, Salvador García, and Francisco Herrera. Self-labeled techniques for semi-supervised learning: taxonomy, software and empirical study. *Knowledge and Information systems*, 42(2):245–284, 2015.
- [29] Rifai Salah, P Vincent, X Muller, et al. Contractive auto-encoders: Explicit invariance during feature extraction. In *Proc. of the 28th International Conference on Machine Learning*, pages 833–840, 2011.
- [30] Dumitru Erhan, Aaron Courville, Yoshua Bengio, and Pascal Vincent. Why does unsupervised pre-training help deep learning? In *Proceedings of the thirteenth international conference on artificial intelligence and statistics*, pages 201–208. JMLR Workshop and Conference Proceedings, 2010.
- [31] Marc’Aurelio Ranzato and Martin Szummer. Semi-supervised learning of compact document representations with deep networks. In *Proceedings of the 25th international conference on Machine learning*, pages 792–799, 2008.
- [32] Jason Weston, Frédéric Ratle, Hossein Mobahi, and Ronan Collobert. Deep learning via semi-supervised embedding. In *Neural networks: Tricks of the trade*, pages 639–655. Springer, 2012.
- [33] Salah Rifai, Grégoire Mesnil, Pascal Vincent, Xavier Muller, Yoshua Bengio, Yann Dauphin, and Xavier Glorot. Higher order contractive auto-encoder. In *Joint European conference on machine learning and knowledge discovery in databases*, pages 645–660. Springer, 2011.
- [34] Takeru Miyato, Shin-ichi Maeda, Masanori Koyama, and Shin Ishii. Virtual adversarial training: a regularization method for supervised and semi-supervised learning. *IEEE transactions on pattern analysis and machine intelligence*, 41(8):1979–1993, 2018.
- [35] Javiera Castillo-Navarro, Bertrand Le Saux, Alexandre Boulch, Nicolas Audebert, and Sébastien Lefèvre. Semi-supervised semantic segmentation in earth observation: The minifrance suite, dataset analysis and multi-task network study. *Machine Learning*, pages 1–36, 2021.
- [36] Ian Goodfellow, Jean Pouget-Abadie, Mehdi Mirza, Bing Xu, David Warde-Farley, Sherjil Ozair, Aaron Courville, and Yoshua Bengio. Generative adversarial nets. *Advances in neural information processing systems*, 27, 2014.
- [37] Danilo Rezende and Shakir Mohamed. Variational inference with normalizing flows. In *International conference on machine learning*, pages 1530–1538. PMLR, 2015.
- [38] Adrian Spurr, Emre Aksan, and Otmar Hilliges. Guiding infogan with semi-supervision. In *Joint European Conference on Machine Learning and Knowledge Discovery in Databases*, pages 119–134. Springer, 2017.
- [39] Xi Chen, Yan Duan, Rein Houthoofd, John Schulman, Ilya Sutskever, and Pieter Abbeel. Infogan: Interpretable representation learning by information maximizing generative adversarial nets. *Advances in neural information processing systems*, 29, 2016.
- [40] Durk P Kingma, Shakir Mohamed, Danilo Jimenez Rezende, and Max Welling. Semi-supervised learning with deep generative models. *Advances in neural information processing systems*, 27, 2014.
- [41] Pavel Izmailov, Polina Kirichenko, Marc Finzi, and Andrew Gordon Wilson. Semi-supervised learning with normalizing flows. In *International Conference on Machine Learning*, pages 4615–4630. PMLR, 2020.

- [42] C. Miesch, L. Poutier, V. Achard, X. Briottet, X. Lenot, and Y. Boucher. Direct and inverse radiative transfer solutions for visible and near-infrared hyperspectral imagery. *IEEE Transactions on Geoscience and Remote Sensing*, 43(7):1552–1562, 2005.
- [43] Guillaume Roussel, Christiane Weber, Xavier Briottet, and Xavier Ceamanos. Comparison of two atmospheric correction methods for the classification of spaceborne urban hyperspectral data depending on the spatial resolution. *International Journal of Remote Sensing*, 39(5):1593–1614, December 2017.
- [44] Jean-Philippe Gastellu-Etchegorry, Eloi Grau, and Nicolas Lauret. Dart: A 3d model for remote sensing images and radiative budget of earth surfaces. *Modeling and simulation in engineering*, (2), 2012.
- [45] Nicolas Audebert, Bertrand Le Saux, and Sébastien Lefèvre. Deep learning for classification of hyperspectral data: A comparative review. *IEEE geoscience and remote sensing magazine*, 7(2):159–173, 2019.
- [46] Yarin Gal and Zoubin Ghahramani. Dropout as a bayesian approximation: Representing model uncertainty in deep learning. In Maria Florina Balcan and Kilian Q. Weinberger, editors, *Proceedings of The 33rd International Conference on Machine Learning*, volume 48 of *Proceedings of Machine Learning Research*, pages 1050–1059, New York, New York, USA, 20–22 Jun 2016. PMLR.
- [47] Diederik P Kingma and Jimmy Ba. Adam: A method for stochastic optimization. *arXiv preprint arXiv:1412.6980*, 2014.
- [48] Julian Zaidi, Jonathan Boilard, Ghyslaine Gagnon, and Marc-André Carbonneau. Measuring disentanglement: A review of metrics. *CoRR*, abs/2012.09276, 2020.
- [49] Kien Do and Truyen Tran. Theory and evaluation metrics for learning disentangled representations, 2019.
- [50] Ricky T. Q. Chen, Xuechen Li, Roger B Grosse, and David K Duvenaud. Isolating sources of disentanglement in variational autoencoders. In S. Bengio, H. Wallach, H. Larochelle, K. Grauman, N. Cesa-Bianchi, and R. Garnett, editors, *Advances in Neural Information Processing Systems*, volume 31. Curran Associates, Inc., 2018.

## Appendix

### A Hybrid model likelihood

In section 3.2, we defined the likelihood of our model as follows:

$$p_\theta(x|y, z_P, z_A) := \frac{1}{Z} f(x) \mathcal{S}(x) \quad (27)$$

where  $f(x) = \mathcal{N}(x|f_P(f_A(y, z_A), z_P), \sigma^2 I)$ ,  $\mathcal{S}(x) = \exp(-\lambda \arccos(\frac{x^T \mu}{\|x\| \|\mu\|}))$  with  $\sigma, \lambda \in \mathbb{R}$  some hyperparameters and  $Z$  a finite constant such that the density integrates to one. Let us prove that such a constant  $Z := \int f(x) \cdot \mathcal{S}(x) dx$  exists.

First, we can easily show that  $f : [0, 1]^B \rightarrow \mathbb{R}$  is square-integrable, as well as  $\mathcal{S} : [0, 1]^B \rightarrow \mathbb{R}$ :

$$\int |\mathcal{S}(x)|^2 dx = \int_{[0,1]^B} \exp(-2\lambda \arccos(\frac{x^T \mu}{\|x\| \|\mu\|})) dx \leq \int_{[0,1]^B} dx = 1 \quad (28)$$

since  $\exp(-2\lambda \arccos(\frac{x^T \mu}{\|x\| \|\mu\|})) \leq 1$  for all  $\mu, x \in [0, 1]^B$ . Moreover,  $f$  and  $\mathcal{S}$  being continuous over  $[0, 1]^B$ , the Cauchy-Schwarz inequality implies that:

$$\left| \int f(x) \cdot \mathcal{S}(x) dx \right| \leq \left( \int f(x)^2 dx \right)^{\frac{1}{2}} \left( \int \mathcal{S}(x)^2 dx \right)^{\frac{1}{2}} = C \in \mathbb{R} \quad (29)$$

Thus,  $Z \in \mathbb{R}$  and  $p_\theta(x|y, z_P, z_A)$  properly defines a probability density function.

### B Models architectures

Models architectures are illustrated in Fig. 9. Every hidden dense layers have 256 neurons. Convolution layers of the classifier have kernels of size  $B_i/5$  along the spectral dimension for the  $i^{th}$  continuous spectral segment. Convolution layers of every encoders have kernels of size 11, 9, 7 and 5 along the spectral dimensions.

### C Earth-atmosphere coupling and neighbouring contributions

To account for the Earth-atmosphere coupling and neighbouring contributions, we simulated a test hyperspectral image with the DART [44] software. The test image has the same optical properties than the train image but a larger noise and a different topography (mostly steeper roofs and more shadows). Besides, we simulated two identical scenes: one with the Earth-atmosphere coupling and one without. Qualitative results on Fig. 11 show that neglecting the Earth-atmosphere coupling and neighbouring contributions in the physical model of p<sup>3</sup>VAE have very little influence on its performances. Actually, p<sup>3</sup>VAE reached a 0.85 and a 0.84 averaged F1 scores on the test image with and without coupling, respectively. We note that the average F1 score is below the one reached on the individual spectra test data set (see section 5) mainly because the F1 score of the sheet metal class brought down the average. As a matter of fact, pixels of sheet metal on the test image are mostly in the shadows, which is a difficult configuration.

#### C.1 Reflectance estimates by the physics-guided VAE

Fig. 10 shows estimated reflectance spectra by the physics-guided VAE. The spectra are clearly unrealistic.

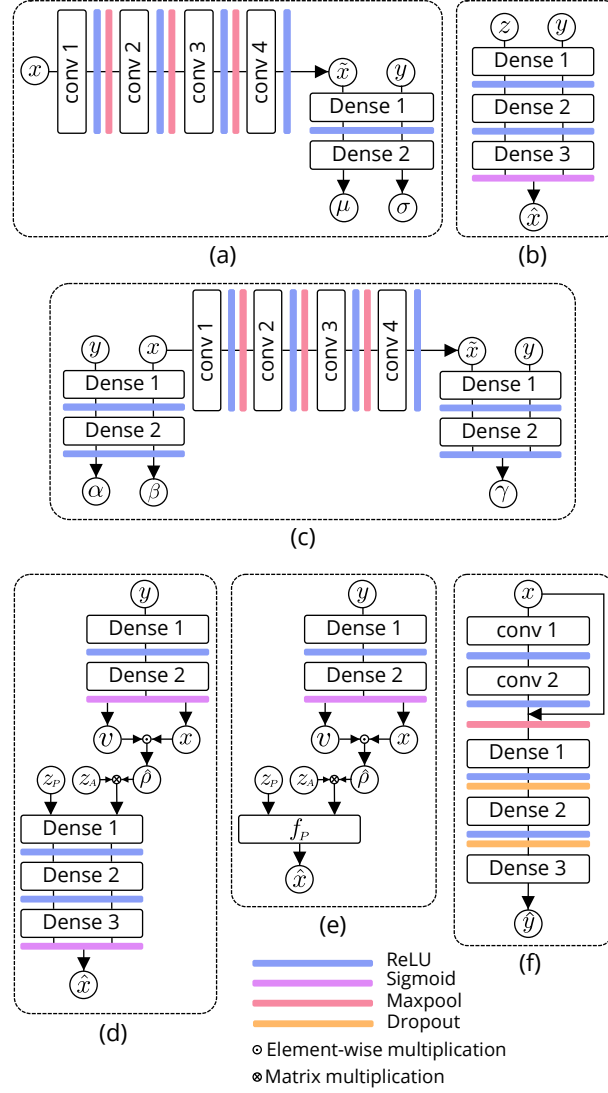


Figure 9: Architecture of the (a) gaussian encoder, (b) gaussian decoder, (c) physics encoder, (d) physics-guided decoder, (e) physics decoder and (f) classifier. The gaussian VAE is the combination of (a)+(b)+(f). The physics-guided VAE is the combination of (c)+(d)+(f). p<sup>3</sup>VAE is the combination of (c)+(e)+(f). The CNN is (f) only.

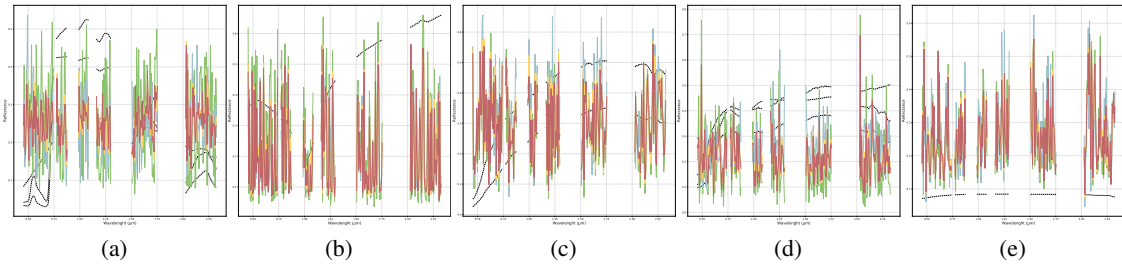


Figure 10: Estimated class reflectance for (a) vegetation, (b) sheet metal, (c) sandy loam, (d) tile and (e) asphalt with the physics-guided VAE. True reflectance spectra, that were used for data simulation, are plotted in dashed black lines.

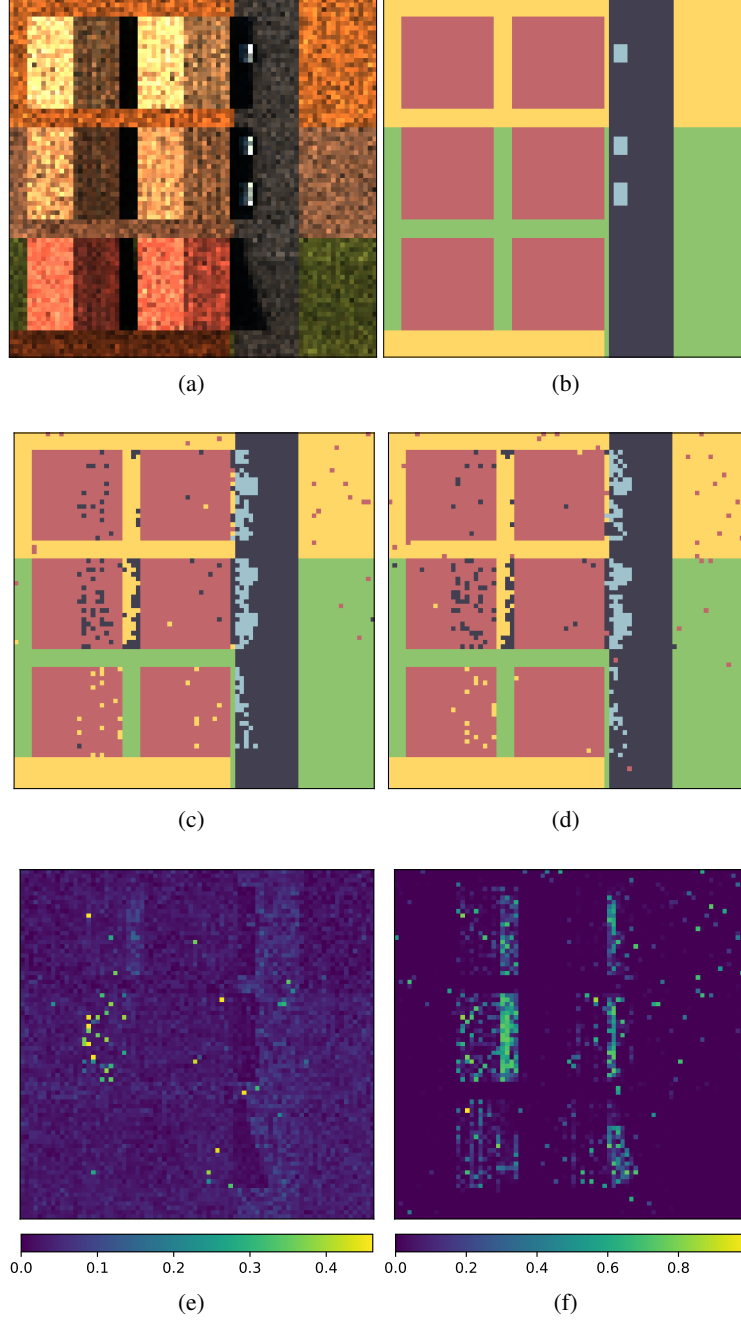


Figure 11: (a) False color composition of the simulated hyperspectral test image without Earth-atmosphere coupling and its (b) ground truth. Predictions on the test image (c) without and (d) with coupling. (e) Empirical standard deviation of  $z_P$  and (f) entropy of the classifier  $q_\phi(y|x)$  on the test image with coupling.